Operational Validation of the MOPITT Instrument Optical Filters*

M. N. DEETER, G. L. FRANCIS, D. P. EDWARDS, AND J. C. GILLE

Atmospheric Chemistry Division, National Center for Atmospheric Research, Boulder, Colorado

E. MCKERNAN AND JAMES R. DRUMMOND

Department of Physics, University of Toronto, Toronto, Ontario, Canada

(Manuscript received 23 November 2001, in final form 8 May 2002)

ABSTRACT

Optical bandpass filters in the Measurements of Pollution in the Troposphere (MOPITT) satellite remote sensing instrument selectivity limit the throughput radiance to absorptive spectral bands associated with the satellite-observed trace gases CO and CH_4. Precise specification of the spectral characteristics of these filters is required to optimize retrieval accuracy. The effects and potential causes of spectral shifts in the optical bandpass filter profiles are described. Specifically, a shift in the assumed bandpass profile produces a relative bias between the calibrated satellite radiances and the corresponding values calculated by an instrument-specific forward radiative transfer model. Conversely, it is shown that the observed bias (as identified and quantified using operational MOPITT satellite radiance data) can be used to determine the relative spectral shift between the nominal (prelaunch) filter profiles and the true operational (in orbit) profiles. Revising both the radiance calibration algorithm and the forward radiative transfer model to account for the revised filter profiles effectively eliminates the radiance biases.

1. Introduction

The Measurements of Pollution in the Troposphere (MOPITT) remote sensing instrument was launched on 18 December 1999 aboard the EOS *Terra* satellite (Drummond et al. 1999; Gille et al. 1999). Based on the principles of gas correlation radiometry, MOPITT was designed to independently measure tropospheric carbon monoxide (CO) and methane (CH_4). This paper describes a technique developed for validating the MOPITT optical bandpass filter profiles by comparing operational (i.e., in orbit) MOPITT radiance data with calculations made using a fast forward radiative transfer model. The main body of the paper begins with a general overview of the operating principles of the instrument. Characteristics of the instrument's optical bandpass filters are then described in detail, with emphasis on the sources of uncertainty in the filters' absolute spectral characteristics. Next, we describe how both the MOPITT radiance calibration algorithm and forward radiative transfer model explicitly depend on the assumed filter profiles. Errors in the filters' spectral characteristics result in relative biases between calibrated satellite radiances and corresponding model-calculated radiances, which in turn result in retrieval errors. The experimental section of the paper begins with the rationale for deducing the operational filter characteristics using satellite radiance data, followed by a description of the actual technique for determining the operational filter shifts. Finally, the effects of incorporating the experimentally determined filter shifts into the radiance calibration algorithm and forward radiative transfer model are demonstrated.

2. Operating principles of the MOPITT instrument

The physical basis of MOPITT's ability to detect tropospheric CO and CH_4 lies in the principles of gas correlation radiometry. Modulation cells containing each of the target gases act as high-spectral resolution optical filters. The filtering characteristics of the cells vary dynamically by modulation of either 1) the cell pressure (Taylor 1983) as in a pressure-modulated cell (PMC), or 2) the optical path length through the absorbing gas (Tolton and Drummond 1997); as in a length-modulated cell (LMC). In both types of cells, the applied modulation has the effect of varying the spectral absorption (and emission) only in the vicinity of the absorption

* The National Center for Atmospheric Research is sponsored by the National Science Foundation.

Corresponding author address: M. N. Deeter, National Center for Atmospheric Research, P.O. Box 3000, Boulder, CO 80307.
E-mail: mnd@eos.ucar.edu

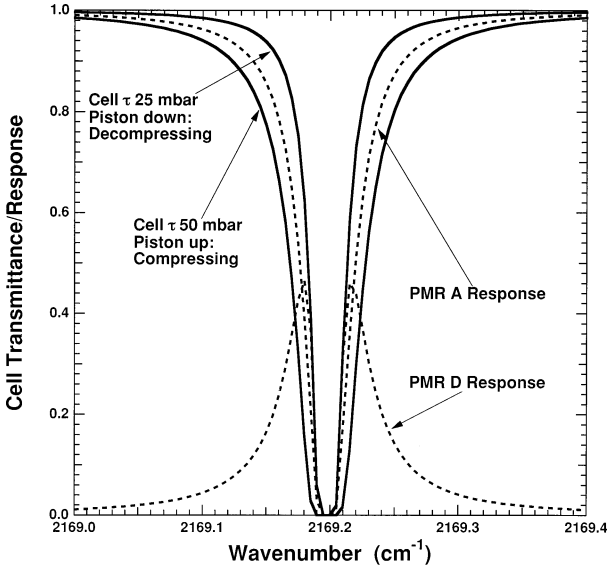

FIG. 1. Transmittance for PMC (channel 7) states of min and max absorption near one CO absorption line, and corresponding A- and D-signal response functions.

lines of the gas contained in the cell. The spectral transmittance near a single CO absorption line for the states of minimum and maximum optical absorption of a CO PMC is shown in Fig. 1. As the pressure in the cell increases, the transmittance in the wings of the CO absorption line decreases.

Measurements of the transmitted optical intensity in the modulation cell states of minimum and maximum cell absorption are combined to form two synthetic signals. The average signals (or ''A signals'') and difference signals (''D signals'') are calculated, respectively, by taking the mean and the difference of the measured radiances in the cell states of minimum and maximum absorption. The equivalent spectral response functions of these synthesized signals are described by the A- and D-signal response functions shown for a single CO absorption line in Fig. 1. The A-signal response is dominated by the spectral regions between the target gas absorption lines, where the mean response is high. In these spectral regions, surface temperature dominates as the source of signal variability, and sensitivity to the target gas is insignificant (Wang et al. 1999). Alternatively, the D-signal response is highest near the absorption line. These signals are relatively much more sensitive to atmospheric target gas concentrations than the A signals. The spectral position of the maximum of the D-signal response function will depend on the particular type and operating parameters of the modulation cell. For example, increasing the absorption depth for both the minimum and maximum cell absorption states will tend to push the D-signal response function maxima farther into the line wings and away from the line center.

A maximum likelihood–based retrieval algorithm (Pan et al. 1998) and a fast radiative transfer model

TABLE 1. Thermal-channel modulator characteristics.

Channel	Modulator type	Cell pressure (mb)
1	Length	200
3	Pressure	50–100
5	Length	800
7	Pressure	25–50

(Edwards et al. 1999) are used to invert the measured A and D signals to determine the tropospheric trace gas concentrations. Retrievals of methane are based on two A signals and two D signals in a band around 2.2 μm, and depend on solar radiation reflected from the earth's surface. Retrievals of CO involve up to 12 measured signals in two distinct bands: a solar reflectance band near 2.3 μm, and a thermal emission band near 4.6 μm. The thermal band signals, which are the subject of this study, are sensitive to thermal emission from the earth's surface as well as atmospheric absorption and emission. Measurements of the CO thermal band signals allow retrievals of CO even for nighttime orbital segments (unlike methane).

Four CO modulation cells (including two PMCs and two LMCs) generate the four thermal band A signals and four thermal band D signals. Corresponding A and D signals derived from the same optical path together constitute one channel of the instrument. Characteristics of the four MOPITT thermal band CO channels and corresponding modulation cells are listed in Table 1. Because of the varying functional characteristics of the four modulation cells, each of the D-signal response functions is dominated by a slightly different spectral region relative to the CO absorption lines. Consequently, the four thermal band D signals are each sensitive to CO in effectively different (but overlapping) layers of the troposphere (Pan et al. 1995). This feature is the basis of MOPITT's ability to resolve the CO vertical profile. Associated with each instrument channel is an optical bandpass filter, which excludes radiance outside the spectral band containing the selected target gas absorption lines.

The MOPITT optical detectors are arranged in a linear array of four pixels onto which a nearly rectangular region of the earth's surface is imaged. Generally, the rays that form this image do not pass through the optical bandpass filters at normal incidence. The point midway between the inner two pixels of the array lies on the optical axis of the system. Therefore, the mean incident angle of rays passing through the bandpass filters will be somewhat smaller for rays that come to a focus on the inner two detector elements than for the outer two detector elements. As described below, this is significant because the spectral transmittance characteristics of optical interference filters generally depend on the incident angle of radiation. This dependence results in effectively

different spectral bandpass profiles for the inner and outer pixels.

As described below in detail, both the A and D signals are calibrated in terms of integrated radiance (in units of W m^{-2} sr^{-1}). Throughout the rest of this paper, the term ''satellite radiance'' refers to calibrated values of the integrated radiance in an earth-viewing geometry. The terms ''blackbody radiance'' and ''space-view radiance'' used in section 4 refer specifically to calibrated values of the integrated radiance in calibration-mode geometries. Finally, the term ''model-calculated radiance'' refers to radiance values generated by the MOPITT operational forward model, which are meant to simulate observed satellite radiances (i.e., in the earth-viewing geometry).

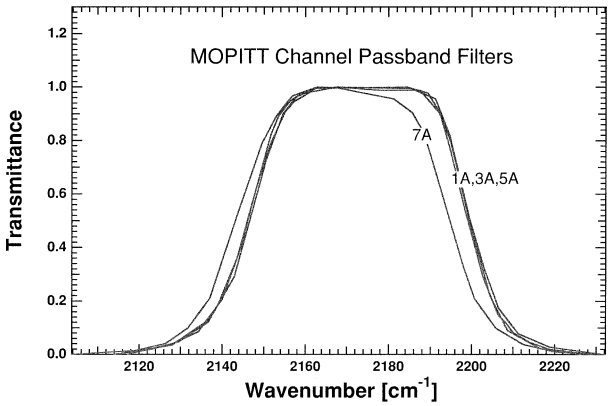

FIG. 2. Nominal thermal-channel filter profiles for MOPITT (measured at 105 K). Labels 1A, 3A, 5A, and 7A refer to MOPITT thermal band A signals for channels 1, 3, 5, and 7, respectively.

3. Optical filter characteristics

The MOPITT interference filters consist of multiple dielectric layers deposited on either silicon or quartz substrates. The transmission characteristics of multilayer bandpass filters are sensitive to the angle of incidence as well as to the thickness and refractive index of the layers (Lissberger and Wilcock 1959). Generally, filter characteristics shift toward shorter wavelengths as the angle of incidence increases and as the filter temperature decreases (Baker and Yen 1967). The angle of incidence effect arises because the optical path difference between multiple reflections decreases as the filter is tilted away from normal incidence. The temperature sensitivity is the net effect of thermal expansion and temperature dependence of the index of refraction. These two effects are typically of opposite sign, although the latter effect is larger than the former for most common filter materials. Both the temperature sensitivity and incident angle sensitivity depend upon the specific design of the filter.

The filter manufacturer measured each of the filters' transmittance at normal incidence with a Perkin–Elmer 983 spectrophotometer (f/4.2) at temperatures of 300 K ($\pm$2 K), 105 K, and again at 300 K (to observe the effects of thermal cycling). In addition, the manufacturer provided temperature sensitivity and angle sensitivity data from which the filter behavior can be estimated for deviations of temperature and angle of incidence. The manufacturer claimed an accuracy of better than 0.5% in these sensitivity values. (Operational deviations of filter temperature and incident angle were well within limits for which these sensitivity values should be valid.)

Filter transmittance profiles measured by the manufacturer at 105 K are shown in Fig. 2. The zero transmission signal level was set manually by the operator for each filter, with an associated error as large as a few percent. Compared to the filter response measured at 105 K, the transmittance profiles measured at 300 K are shifted toward longer wavelengths (lower frequency) and are decreased in amplitude, whereas the shapes of the profiles are relatively unchanged. This spectral shift is consistent with the manufacturer-provided temperature filter shift coefficient for this filter (0.457 nm K^{-1}), whereas the higher transmittance at 105 K is the result of operating the filter closer to its design temperature (between 85 and 92 K). Considering all possible sources of experimental error, we estimate the uncertainty in the tabulated frequency values in the filter transmittance profiles to be $\pm$2 cm^{-1}, and of the transmittance to be $\pm$3% of the peak transmittance value.

As indicated previously, rays that come to focus on the inner and outer pixels of the MOPITT optical detector are associated with different angles of incidence with respect to the optical filters. Based on results of a ray-tracing analysis, mean angles of incidence of 2° and 5.6° were calculated for the inner and outer pixels, respectively. The angle of incidence uncertainty was estimated as 25% of the calculated mean angle of incidence. The sensitivity of the filter properties to angle of incidence was modeled according to the monolayer approximation (Pidgeon and Smith 1964). According to this model, the filter shift $\Delta\nu_\phi$ for an incident angle ϕ is calculated according to the equations

$$\frac{\Delta\nu_\phi}{\nu_0} = \sec(\phi^*) - 1 \quad \text{and} \tag{1}$$

$$\sin(\phi^*) = \frac{\sin(\phi)}{n^*}, \tag{2}$$

where n^* is the filter's effective refractive index (provided by the manufacturer) and ν_0 is the nominal (unshifted) frequency. Table 2 lists the calculated temperature and angle of incidence filter shifts for the inner and outer pixels for each of the thermal channels. The shifts associated with the temperature difference between the laboratory measurements (105 K) and the operational filter temperatures (87–92 K) are much greater than the shifts due to the incident angle effect.

Absolute accuracy in the spectral specification of the operational bandpass filter profiles is important for two

TABLE 2. Theoretical spectral shifts due to filter temperature dependence ($\Delta\nu_T$), incident angle dependence ($\Delta\nu_\phi$), and their sum ($\Delta\nu_{\text{thy}}$). (All spectral shifts are reported in units of cm^{-1}.)

Channel	Pixel type	$\Delta\nu_T$	$\Delta\nu_\phi$	$\Delta\nu_{\text{thy}}$
1	Inner	2.80	0.13	2.93
	Outer	2.80	1.02	3.82
3	Inner	2.84	0.13	2.97
	Outer	2.84	1.02	3.86
5	Inner	3.91	0.13	4.04
	Outer	3.91	1.02	4.93
7	Inner	3.86	0.13	3.99
	Outer	3.86	1.02	4.88

reasons. First, the radiance calibration algorithm, which is used to convert raw satellite data to calibrated radiances, depends on lookup tables based on the assumed filter profiles. As shown below, errors in the satellite radiances will result directly from spectral shifts in the assumed filter profiles. Second, the operational forward model is also developed for particular assumed filter profiles. Thus, errors in the assumed filter profile will produce errors in both the satellite radiances and model calculations. However, these two types of radiance error have fundamentally different physical origins, so that filter profile errors result in a relative bias between the satellite radiances and corresponding model calculations. Small relative radiance errors degrade the quality of the retrieval results while larger errors render the retrievals unstable.

4. Radiance calibration

A primary detector issue considered in the design of the MOPITT instrument was detector response linearity. MOPITT optical detectors were selected based in part on this criterion, and response linearity was verified in laboratory measurements. Thus, for a particular channel, the MOPITT satellite radiance L is calculated from the raw instrument count C, using the gain $\mathcal{G}$ and the offset O, where

$$L \equiv \mathcal{G}C + O. \tag{3}$$

Here $\mathcal{G}$ and O are determined from instrument counts observed during measurements of the internal blackbody (C_I) and space view (C_S). Corresponding radiances are denoted L_I and L_S. The space-view radiance L_S is assumed to be zero. In addition, a precomputed calibration table maps known internal blackbody temperatures to internal blackbody radiances. If the internal blackbody temperature is T_{BB}, with corresponding calculated blackbody radiance $L_I(T_{\text{BB}})$, then the gain $\mathcal{G}$ is

$$\mathcal{G} \equiv \left[\frac{L_I(T_{\text{BB}})}{C_I - C_S}\right]. \tag{4}$$

The offset O, which represents the radiance for an instrument count of zero, is then given by

$$O \equiv -\mathcal{G}C_S. \tag{5}$$

MOPITT satellite radiance calibration errors can therefore arise either through errors in the instrument counts or errors in the calibration table (both of which would directly affect $\mathcal{G}$ and O).

In the calibration table, blackbody radiances L_I are tabulated as a function of T_{BB} using the relation

$$L_{I_i}^{A,D} = \int B_I(\nu, T_{\text{BB}}) w_i(\nu) h_i^{A,D}(\nu)\, d\nu, \tag{6}$$

where, for instrument channel i, $L_{I_i}^{A,D}$ represents the MOPITT A or D internal blackbody signal, $B_I(\nu, T_{\text{BB}})$ is the blackbody (Planck function) spectral radiance, $h_i^{A,D}(\nu)$ is the correlation cell A- or D-signal response (i.e., the effective cell transmittance), and $w_i(\nu)$ is the bandpass filter profile (i.e., the filter transmittance). Emissivity of the blackbody is assumed to be unity over the passband of the optical filters and therefore does not appear in Eq. (6). This assumption is warranted by the very high emissivity specification from the manufacturer (>0.999) for the internal blackbody. Likewise, the spectral dependence of the transmittance (and reflectance) of other optical components in the system (e.g., lenses and mirrors) is assumed to be negligible. The correlation cell A- and D-signal response functions (Fig. 1) are precalculated using the general purpose line-by-line (LBL) transmittance and radiance model GENLN2 (Edwards 1992). Correlation cell A-signal response functions are known to high precision for both the LMCs and PMCs. Modeling uncertainty in PMC characterization affecting the PMC D-signal response functions might be significant, but is not relevant in the present context. In short, errors in the assumed filter profile $w_i(\nu)$ propagate to produce errors in the $L_{I_i}^{A,D}$ values in the MOPITT calibration table [Eq. (6)], which then produce errors in the MOPITT satellite radiances through errors in both the gain [Eq. (4)] and offset [Eq. (5)].

5. Forward modeling

The bandpass filter profile is also required in the MOPITT operational forward radiative transfer model MOPFAS (Edwards et al. 1999). MOPFAS model-calculated radiances $M_i^{A,D}$ are based on the relation

$$M_i^{A,D} = \int I(\nu) w_i(\nu) h_i^{A,D}(\nu)\, d\nu, \tag{7}$$

where $I(\nu)$ is the upwelling top-of-atmosphere (TOA) spectral radiance. A spectral shift of the filter profile $w_i(\nu)$ affects the blackbody radiances $L_{I_i}^{A,D}$ [Eq. (6)] differently than the model-calculated radiances $M_i^{A,D}$ [Eq. (7)]. (In fact, this difference is exploited as the means of determining the error in the assumed optical filter

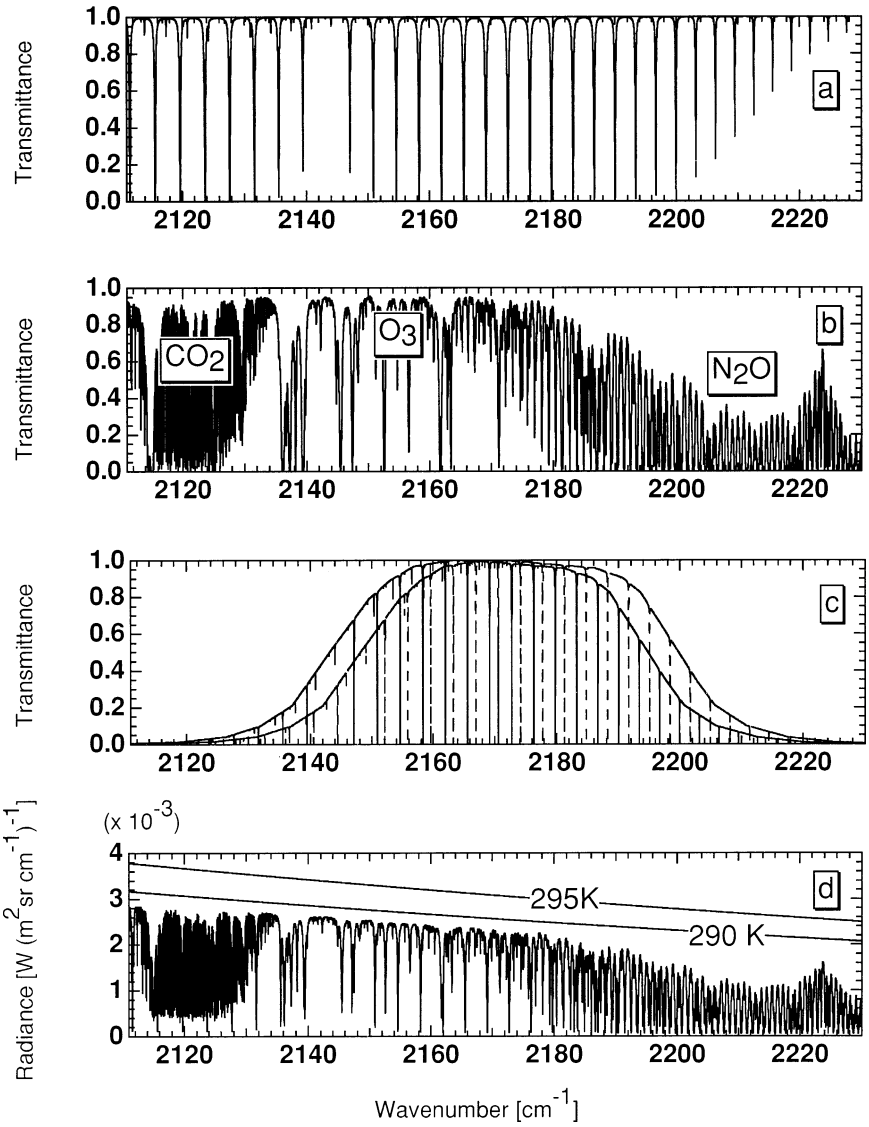

FIG. 3. Atmospheric transmittance (surface to TOA) spectra for (a) CO in the MOPITT thermal passband region and for (b) CO_2, O_3, and N_2O. (c) The instrumental A-signal response (combined bandpass filter transmittance and correlation cell A-signal response) for the nominal filter profile (solid) and the same filter shifted 5 cm^{-1} (dashed). (d) Comparison of a typical TOA radiance spectra with blackbody spectra at 290 K (typical Planck radiance of the earth's surface) and 295 K (a typical radiance of the MOPITT internal warm blackbody). The TOA radiance drop-off at high wavenumber is due to N_2O absorption.

profiles.) As shown in Fig. 3d, $B_I(\nu, T_{BB})$ is a smooth function of frequency whereas the TOA radiance $I(\nu)$ exhibits a complex line structure. In particular, as shown in Fig. 3b and Fig. 3c, a strong N_2O band overlaps the high-wavenumber side of the MOPITT CO thermal-channel passbands. If the bandpass filter profile were shifted to higher wavenumber, the blackbody radiance $L_{I_i}^{A,D}$ would decrease, due to the decrease in blackbody radiation with increasing wavenumber. The model-calculated radiance $M_i^{A,D}$ would also decrease due to the change in blackbody terrestrial and atmospheric radiance. However, $M_i^{A,D}$ would decrease more than $L_{I_i}^{A,D}$ because of the additional effect of enhanced N_2O absorption. This differential change may be roughly quantified by comparing Fig. 4a and Fig. 4b. For a hypothetical filter shift of 6 cm^{-1} (to higher frequency) applied to channel 1, Fig. 4a indicates that $L_{I_1}^{A,D}$ falls by approximately 2%; Fig. 4b shows that $M_1^{A,D}$ falls by about 9% for the same filter shift value, mainly as a consequence of enhanced absorption of upwelling atmospheric radiance in the N_2O band. Thus, in a relative sense, a radiance bias of approximately 7% will result from a filter shift of 6 cm^{-1} applied to the channel-1 filter profile.

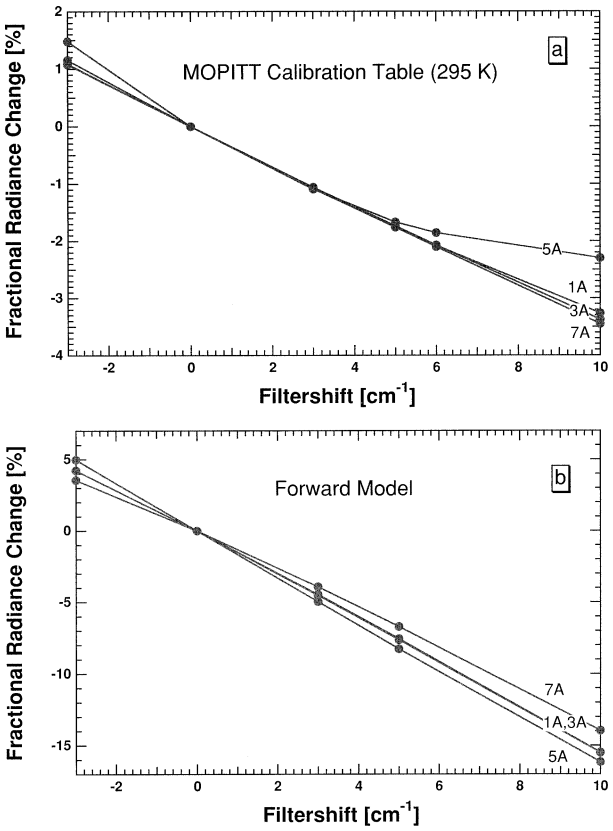

FIG. 4. Calculated filter shift sensitivity of (a) satellite calibration table values and (b) forward model radiances. Curves are shown for the four MOPITT thermal band A signals.

The absolute spectral uncertainty associated with the filter profile measurement was estimated in section 3 as ± 2 cm^{-1}. Additional sources of uncertainty include errors in the assumed operational temperature of the filters, and the assumed angle of incidence. The cumulative degrading effects of these uncertainties on the accuracy of the satellite radiances and model-calculated radiances dictated that the filter profiles be validated operationally. In the following we show that, in particular scenes, radiance biases (as indicated by consistent differences between satellite thermal-channel A signals and corresponding model-calculated radiances) are dominated by uncertainty in the filters' spectral coordinates. Our validation strategy is to quantify these biases and then solve for the corresponding operational filter shifts (i.e., the relative spectral shifts between the nominal filter profiles and the actual in-orbit filter profiles). Comparing these derived filter shift values with the estimated precision of the nominal filter profiles provides a consistency check. In addition to filter shift effects, however, radiance biases might also be the result of errors in either the instrument raw data, errors in one or more of the inputs to the forward model, or errors in the forward model itself. For the purpose of operational filter profile validation, all other potential sources of radiance bias must be analyzed before it is reasonable to conclude that the observed radiance biases are due mainly to filter shift effects.

Systematic errors in the processed instrument counts have been ruled out by examining gain and offset time series from the MOPITT engineering data stream. As a result, systematic errors in the satellite radiances can only arise through errors in the blackbody radiance L_I, which determines the gain G and offset O. Blackbody radiance L_I is given by Eq. (6), where the only significant uncertainty involves the bandpass filter profile $w_i(\nu)$. The blackbody temperature in Eq. (6) is monitored and is found to be stable.

Because of the strong dependence of the model-calculated radiances on the assumed surface temperature, and because of the strong diurnal variability of surface temperature over most land surfaces, only oceanic scenes were considered as the basis for quantifying the radiance biases. Since sea surface temperature (SST) variability (both spatial and temporal) is typically smaller within the Tropics than outside the Tropics, only tropical ocean scenes were used. SST values used in the operational data processing from the National Centers for Environmental Prediction (NCEP) reflect the ''bulk'' SST T_{bulk} at a depth of approximately 1 m, which may differ from the ''skin'' SST T_{skin} (which physically determines the upwelling radiance) by up to 1 K. Because this thermal bias between T_{bulk} and T_{skin} is generally more stable at night than during the day, only cloud-free nighttime, tropical ocean scenes were used to quantify the radiance biases (Schluessel 1990). For these scenes, the mean skin/bulk bias $\langle T_{\text{skin}} - T_{\text{bulk}} \rangle$ is approximately -0.25 K, with an uncertainty of approximately 0.1 K. In the radiative transfer model, this surface temperature uncertainty results in a radiance uncertainty for the A signals of only about 0.2%. The exclusive use of nighttime scenes also has the advantage of preventing radiance contamination by ''sunglint'' effects in which variable amounts of solar radiation may be scattered into the instrument's field of view (Nath et al. 1993).

The MOPITT retrieval algorithm uses the MOPFAS forward model to quickly calculate spectrally integrated radiances while maintaining high accuracy. Approximations in calculating spectrally integrated transmittances, and the radiative transfer, introduce only small errors in MOPFAS when compared to LBL GENLN2 calculations, typically less than 0.03% in the thermal-channel A signals (Edwards et al. 1999). Forward model sensitivities to uncertainties in variable gas concentrations have also been carefully examined. Modeled A signals are very insensitive to plausible uncertainties in concentrations of water vapor, N_2O, CO_2, and O_3, which are the dominant contaminating gases in the MOPITT CO thermal band channels. Relative radiance changes in the thermal channel A signals of $<1\%$ result from a 10% column change in either N_2O, CO_2, or O_3. For water vapor, the relative radiance change is $<0.3\%$. Since the A signals are dominated by the background

TABLE 3. Identification of clear-sky MOPITT scenes used to quantify relative radiance biases. For scenes 1–6, only radiances from nighttime overpasses were analyzed. Scenes 7a,b (over the northern Pacific Ocean) were used to demonstrate geographic generality of experimentally determined filter shift values (see section 6).

		Lat limits		Lon limits		
Scene	Date	Min	Max	Min	Max	No. pixels
1	14 Mar 2000	5°S	15°N	53°E	73°E	435
2	25 Mar 2000	5°S	15°N	53°E	73°E	431
3	6 Apr 2000	5°S	15°N	53°E	73°E	307
4	27 Apr 2000	5°S	15°N	53°E	73°E	1673
5	5 May 2000	30°S	15°S	90°E	110°E	908
6	4 Jun 2000	15°S	Equator	10°W	10°E	598
7a	23 Aug 2000	30°N	50°N	180°W	130°E	1107 (day)
7b	23 Aug 2000	30°N	50°N	180°W	130°E	1483 (night)

radiance contribution between the target gas (CO) absorption lines, and since the High-Resolution Transmission Molecular Absorption Database (HITRAN) CO line parameters (Rothman et al. 1998) are generally well established in the MOPITT thermal-channel passbands, the modeled A signals are insensitive to uncertainties in the line parameters (Edwards et al. 1999). (The dominating effect of the background radiance in the thermal-channel A signals also greatly minimizes modeling errors associated with the line-by-line model against which MOPFAS is compared.) The forward radiative transfer model implicitly assumes clear-sky conditions, and thus does not account for the possible effects of undetected clouds or aerosols. However, the contaminating effects (in terms of radiance bias) of undetected clouds and aerosols should be expected to be highly variable in both space and time. As will be demonstrated, the radiance biases for the selected scenes are quite consistent, indicating the lack of significant contamination by (or variability of) either undetected clouds or aerosols.

The MOPITT validation plan (available online at www.eos.ucar.edu/mopitt/validation/index.html) includes several components related to radiance validation. Unfortunately, however, validation of the operational filter profiles is not addressed in the validation plan. Moreover, the components in the plan related to radiance validation focus on validation of the LMC and PMC D signals (which are not relevant here). Thus, a novel methodology was developed to quantify the A-signal radiance biases as a preliminary step to determination of the optical filter shifts. For convenience, relative radiance biases r were expressed as ratios of the satellite radiances and the corresponding model-calculated radiances. For each satellite observation (or ''pixel''), r values were calculated for each of the four thermal band A signals. If $L(\Delta\nu)$ and $M(\Delta\nu)$ are, respectively, the satellite radiance and corresponding model-calculated radiance for a specific filter shift $\Delta\nu$, then the observed relative radiance bias is given by

$$r \equiv \frac{L(0)}{M(0)}. \tag{8}$$

A null filter shift ($\Delta\nu = 0$) represents the nominal filter profile, which we take as the measured (105 K) filter profile (not including predicted incident-angle or temperature sensitivity effects).

Model-calculated radiances were based on NCEP meteorological data, and on NCEP SST values decreased by 0.25 K to account for the skin/bulk SST effect described previously. The effects of cloud contamination on the analysis of radiance biases were prevented by a threshold-based radiance prefilter (Warner et al. 2001) and were verified visually and statistically. Histograms of the relative radiance biases were generated for each scene. The observed general symmetry of the radiance bias distributions for each scene is consistent with a lack of clouds, since clouds over the ocean generally reduce the upwelling thermally emitted infrared radiation relative to clear-sky conditions. Thus, cloud-contaminated scenes are characterized by longer ''tails'' on the low-radiance end of the radiance distribution, which were not observed.

Six cloud-free, nighttime scenes over tropical oceans were selected as the basis for quantifying the radiance biases and are described in Table 3. Because of the filters' incident-angle dependence, radiance biases for inner and outer pixels were analyzed separately. Radiance bias histograms produced for each scene were all qualitatively similar. Histograms for the entire dataset, split into inner- and outer-pixel subsets, are shown in Fig. 5. During the overall period between the first (14 March 2000) and last (4 June 2000) of these scenes, no significant trend was observed in the biases. A total of 4352 MOPITT pixels resulted when radiances from all six scenes were combined. Median radiance bias statistics (which are less sensitive to anomalous ''outlier'' satellite radiances than mean statistics) were calculated from this set of radiances for all four thermal-channel A signals and are listed in Table 4.

Filter shifts were determined for each MOPITT thermal band channel, and for the inner and outer pixels separately. As described previously, shifts in the filter profile affect both the satellite radiances and forward model calculations, though by different amounts. The

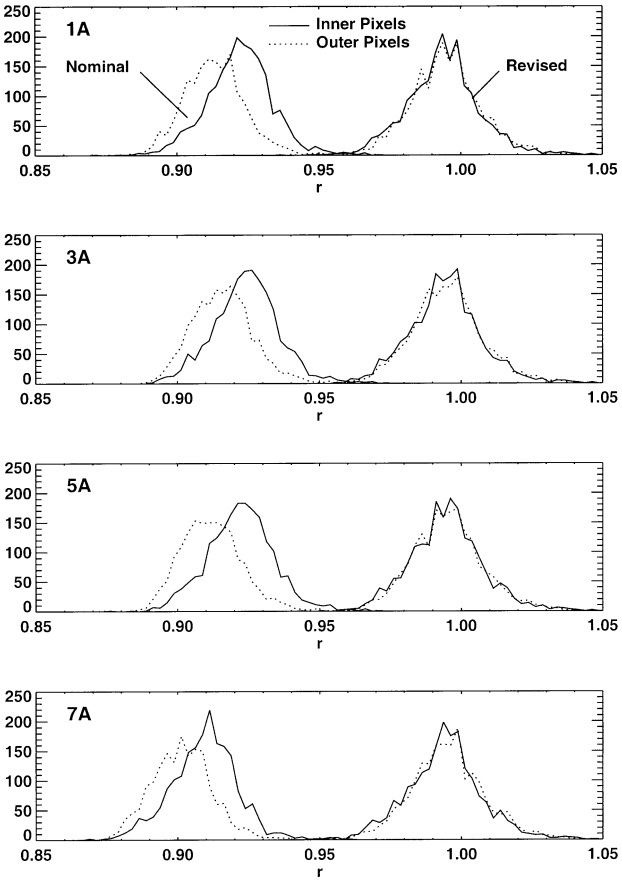

FIG. 5. Histograms of relative radiance biases r observed for MOPITT thermal channels. In each panel, histograms toward left (peaking between 0.90 and 0.95) correspond to bias values obtained using nominal filter profiles whereas histograms toward right (peaking near 1.0) correspond to bias values calculated after revising filter profiles.

actual technique used to determine the filter shifts from the observed radiance biases is described in the appendix. Results of this analysis are presented in Table 4. For each channel, the observed median relative radiance bias r and corresponding spectral shift $\Delta\nu$ are listed for inner and outer pixels separately. In addition, the residual shift $\Delta\nu_{\text{res}}$ is listed in each case, where

$$\Delta\nu_{\text{res}} \equiv \Delta\nu - \Delta\nu_{\text{thy}} \tag{9}$$

and the theoretical shift $\Delta\nu_{\text{thy}}$ is taken from Table 2. Thus, $\Delta\nu_{\text{res}}$ represents the residual component of $\Delta\nu$ not due to the expected effects of filter profile temperature dependence and incident angle effects (as described in section 3). Except for channel 7, $\Delta\nu_{\text{res}}$ values all fall within the estimated uncertainty of the filter profile (± 2 cm^{-1}). For channel 7, the larger value of $\Delta\nu_{\text{res}}$ might be related to the atypical profile shape and position for that filter relative to the filters for the other channels (see Fig. 3).

Due to all the sources of radiance bias not related to the filter profile, the precision of both the satellite radiances and forward model radiances is estimated as approximately 1%. The estimated uncertainty of their ratio r is slightly larger. Previously, it was shown that an A-signal bias of approximately 8% results from a filter shift of 6 cm^{-1}. Thus, due to the uncertainties in the satellite radiance and forward model radiances, the uncertainty in the derived filter shift values is approximately 1 cm^{-1}.

TABLE 4. Relative radiance bias statistics (calculated for MOPITT data from all scenes listed in Table 3) and corresponding total shift and residual shift values. Shifts due to temperature dependence resulted from deviations (nominal minus operational) of 13 K for channels 1 and 3 and 18 K for channels 5 and 7. Shifts due to incident angle resulted from deviations (relative to normal incidence) of 2° for inner pixels and 5.6° for outer pixels. (All spectral shifts are reported in units of cm^{-1}.) Estimated uncertainty of $\Delta\nu$ and $\Delta\nu_{\text{res}}$ is 1.0 cm^{-1}.

Channel	Pixel type	r	$\Delta\nu$	$\Delta\nu_{\text{res}}$
1	Inner	0.921	4.8	1.9
	Outer	0.912	5.7	1.9
3	Inner	0.923	4.7	1.7
	Outer	0.915	5.6	1.7
5	Inner	0.920	4.5	0.4
	Outer	0.910	5.4	0.5
7	Inner	0.908	6.9	2.9
	Outer	0.901	7.8	2.9

6. Verification of revised filter profiles

Revised filter profiles were constructed for each thermal channel (separately for inner and outer pixels) by applying the experimentally determined filter shift values $\Delta\nu$ to the corresponding nominal filter profiles. These adjusted filter profiles were then incorporated into revised versions of both the satellite radiance calibration algorithm and the forward radiative transfer model, as described previously. Finally, new satellite radiances and forward model-calculated radiances were generated for the same set of scenes (Table 3) previously used to quantify the relative radiance biases. Radiance bias histograms were calculated for the new satellite radiances and corresponding model calculations. As shown in Fig. 5, the median relative radiance bias values obtained using the revised algorithms are very close to 1.00 for all channels. Furthermore, histograms for inner- and outer-pixel subsets overlap with no apparent relative bias.

Bias values for channel 1 obtained using the nominal filter profile are compared with values obtained using the revised filter profiles in Fig. 6. Data are shown for scene 4 (described in Table 3). As expected, the original general bias of approximately 1.0×10^{-2} W m^{-2} sr^{-1} apparent in Fig. 6a is greatly reduced in the bias values for the revised filter profiles, shown in Fig. 6b.

The presented analysis assumes the original source of the observed radiance biases to be instrumental, and

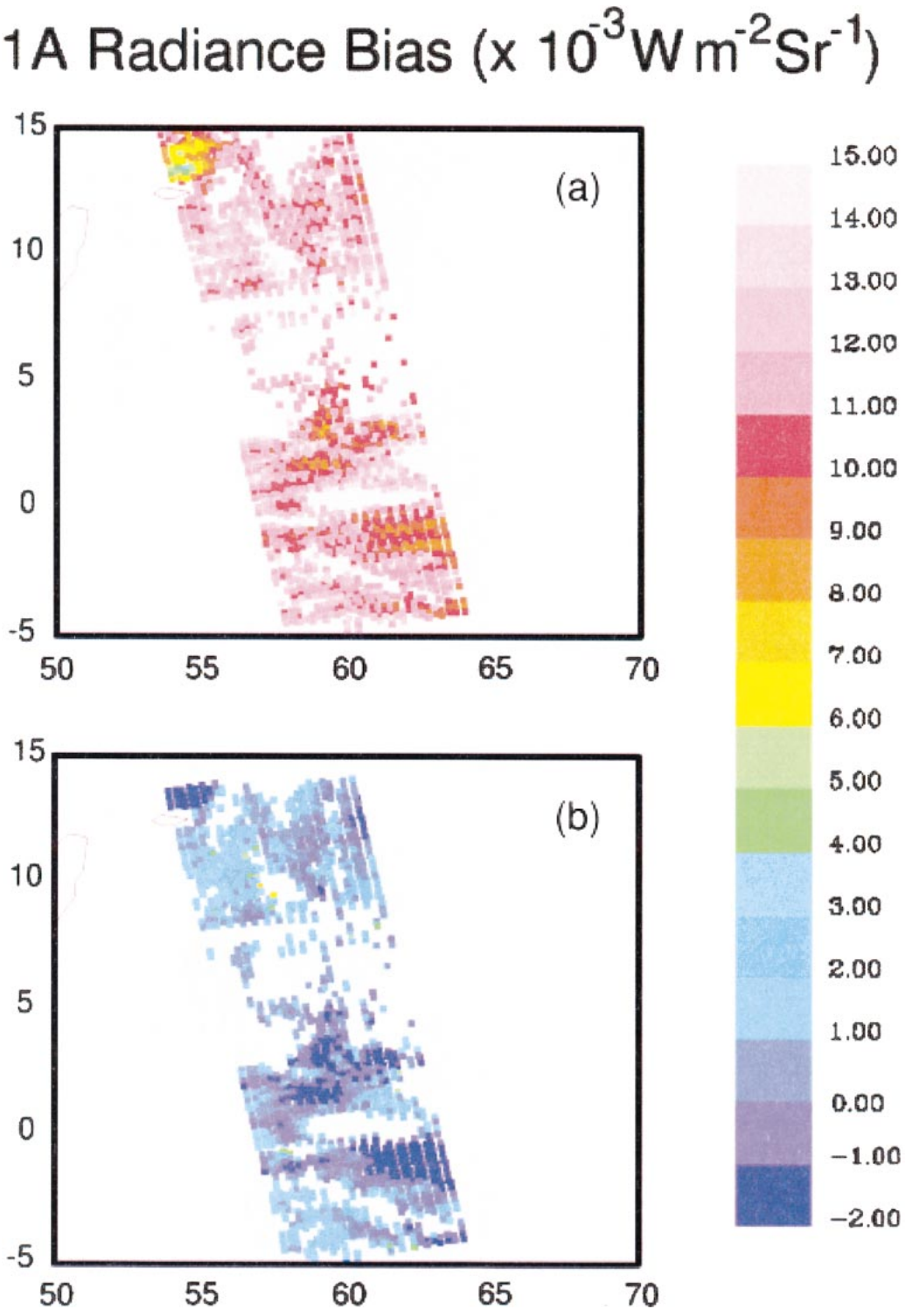

FIG. 6. Radiance bias (model-calculated radiance *M* minus satellite radiance *L*) for Indian Ocean scene on 27 Apr 2000 as determined using (a) nominal filter profiles and (b) revised filter profiles.

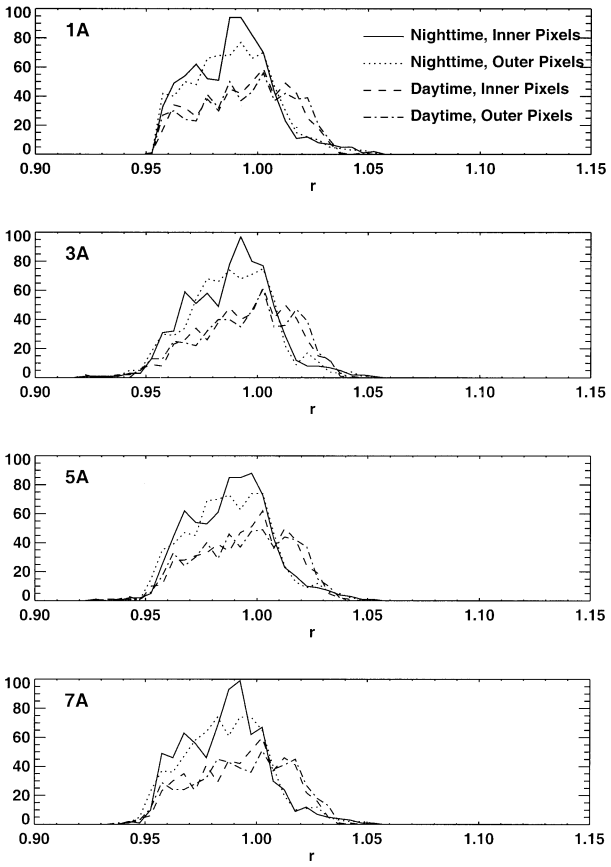

FIG. 7. Histograms of relative radiance biases *r* observed for daytime (scene 7a) and nighttime (scene 7b) MOPITT overpasses over northern Pacific Ocean on 23 Aug 2000 (see Table 3). Shown histograms describe biases observed after incorporation of revised filter profiles into radiance calibration algorithm and forward model.

not geophysical. If this assumption is valid, the experimentally determined filter shift values must be valid globally. Thus, the geographical generality of the the experimentally determined filter shift values was checked by comparing satellite and model-calculated radiances over the northern Pacific Ocean. This scene, described as scene 7 in Table 3, contrasts sharply (in terms of both surface temperature and atmospheric state) with the tropical scenes for which the filter shift values were determined. Histograms of relative radiance biases *r* observed for daytime (scene 7a) and nighttime (scene 7b) MOPITT overpasses over the northern Pacific Ocean are shown in Fig. 7. Compared to the revised-profile histograms in Fig. 5, these histograms appear broader (probably indicating larger random errors between predicted and actual surface temperatures) and less symmetric (possibly due to the effects of undetected clouds). However, in agreement with Fig. 5, there is no apparent bias between inner and outer pixels and all of the histograms peak within about 1% of unity (the expected value). These results are therefore consistent with the hypothesis that the original observed radiance biases are due to filter shift effects.

7. Conclusions

Radiance errors, both systematic and random, often limit the performance of remote sensing systems. Provided that they can be quantified statistically, the effect of random errors can be minimized through the use of retrieval algorithms (including the maximum likelihood technique), which explicitly account for such errors. Systematic errors, however, usually indicate problems in either the instrument model (which is needed to develop the radiance calibration algorithm) or the forward radiative transfer model. Optimization of the performance of the remote sensing retrieval algorithm demands that systematic radiance errors be identified and eliminated.

Differences between the optical filter profiles assumed in the data processing algorithms (radiance calibration and forward modeling) and the true operational filter profiles appear to be the primary source of biases between the observed satellite radiances and corresponding model-calculated radiances. Relative spectral shifts of the operational filter profiles (relative to the nominal filter profiles) may arise due to various effects including filter temperature variability, incident angle effects, and laboratory profile measurement error. Accordingly, we have developed a methodology to accurately quantify the radiance biases in the MOPITT thermal channel A signals and use that information to determine the relative spectral shifts between the nominal prelaunch measured filter profiles and the effective operational filter profiles.

MOPITT satellite radiances and corresponding model-calculated radiances from six cloud-free nighttime scenes over tropical oceans were analyzed to quantify the relative radiance biases for each of the four MOPITT thermal channels. Statistics were calculated for the inner and outer pixels separately because of incident-angle effects on the operational filter profiles. A numerical technique for solving for the spectral profile shifts corresponding to the observed radiance biases was developed and applied. In all cases examined, the residual filter shift (obtained by subtracting the calculable effects of temperature and incident angle from the total filter shift) was less than or very close to the estimated uncertainty in the filter profiles' spectral values. Finally, the nominal filter profiles were corrected and incorporated into revised versions of the radiance calibration algorithm and forward radiative transfer model.

Acknowledgments. The University of Toronto MOPITT team would like to acknowledge the Canadian Space Agency (CSA) for the instrument finance, the Natural Sciences and Engineering Research Council (NSERC) and Meteorological Service of Canada (MSC) for help with the data processing, COMDEV (the prime

contractor), ABB BOMEM, and the University of Toronto. The NCAR MOPITT team would like to thank D. Ziskin, C. Cavanaugh, and L. Mayer for data processing support and G. Wick (NOAA) and J. Warner (NCAR) for valuable discussions. The NCAR MOPITT project is supported by the National Aeronautics and Space Administration (NASA) Earth Observing System (EOS) Program.

APPENDIX

Determination of Optical Filter Shift from Observed Radiance Bias

For a particular MOPITT thermal band channel and pixel, $L(\Delta\nu)$ is defined as the satellite radiance as a function of filter shift $\Delta\nu$, and $M(\Delta\nu)$ is the corresponding forward model radiance. As defined in Eq. (8), the observed relative radiance bias r is the ratio of $L(0)$ and $M(0)$.

We then define $\Delta\nu^*$ as the effective filter shift, where

$$L(\Delta\nu^*) = M(\Delta\nu^*) \tag{A1}$$

by definition. The objective of this section is to show that $\Delta\nu^*$ may be determined from the observed relative radiance bias r and tabulated values of the functions $L(\Delta\nu)$ and $M(\Delta\nu)$.

Next, we define two functions,

$$\mathcal{M}(\Delta\nu) = [M(\Delta\nu) - M(0)]/M(0) \quad \text{and} \tag{A2}$$

$$\mathcal{L}(\Delta\nu) = [L(\Delta\nu) - L(0)]/L(0). \tag{A3}$$

Thus, $\mathcal{M}(\Delta\nu)$ is the fractional change in the forward model radiance as a function of filter shift $\Delta\nu$, and $\mathcal{L}(\Delta\nu)$ is the fractional change in the satellite radiance. Both $\mathcal{L}(\Delta\nu)$ and $\mathcal{M}(\Delta\nu)$ are known, precomputed functions and are shown in Figs. 4a and Fig. 4b, respectively. Here $\mathcal{M}(\Delta\nu)$ is computed using a fixed tropical reference atmosphere (characteristic of the scenes used to quantify the radiance biases). Like $L(\Delta\nu)$, $M(\Delta\nu)$, and r, the functions $\mathcal{M}(\Delta\nu)$ and $\mathcal{L}(\Delta\nu)$ are both channel and pixel dependent.

Algebraic manipulation of Eqs. (A1)–(A3) then leads to the equation

$$r = \frac{1 + \mathcal{M}(\Delta\nu^*)}{1 + \mathcal{L}(\Delta\nu^*)}. \tag{A4}$$

Since $\mathcal{M}(\Delta\nu)$ and $\mathcal{L}(\Delta\nu)$ are known (tabulated) functions of $\Delta\nu$, Eq. (A4) shows that $\Delta\nu^*$ may be uniquely determined for a given relative radiance bias r by using any common root-finding technique [such as Newton's method (Press et al. 1986)].

REFERENCES

Baker, M. L., and V. L. Yen, 1967: Effects of the variation of angle of incidence and temperature on infrared filter characteristics. *Appl. Opt.*, **6,** 1343–1351.

Drummond, J. R., and Coauthors, 1999: Early mission planning for the MOPITT instrument. *Proc. SPIE*, **3756,** 396–402.

Edwards, D. P., 1992: GENLN2: A general line-by-line atmospheric transmittance and radiance model, Version 3.0. NCAR Tech. Rep. NCAR/TN-367+STR, 147 pp.

——, C. M. Halvorson, and J. C. Gille, 1999: Radiative transfer modeling for the EOS Terra satellite Measurements of Pollution in the Troposphere (MOPITT) instrument. *J. Geophys. Res.*, **104,** 16 755–16 775.

Gille, J., and Coauthors, 1999: The EOS MOPITT experiment: Extracting the information from the measurements. *Proc. SPIE*, **3756,** 403–408.

Lissberger, P. H., and W. L. Wilcock, 1959: Properties of all-dielectric interference filters II: Filters in parallel beams of light incident obliquely and in convergent beams. *J. Opt. Soc. Amer.*, **49,** 126–130.

Nath, A. N., M. V. Rao, and K. H. Rao, 1993: Observed high temperatures in the sunglint area over the North Indian Ocean. *Int. J. Remote Sens.*, **14,** 849–853.

Pan, L., D. P. Edwards, J. C. Gille, M. W. Smith, and J. R. Drummond, 1995: Satellite remote sensing of tropospheric CO and CH_4: Forward model studies of the MOPITT instrument. *Appl. Opt.*, **34,** 6976–6988.

——, J. Gille, D. P. Edwards, P. L. Bailey, and C. D. Rodgers, 1998: Retrieval of carbon monoxide for the MOPITT instrument. *J. Geophys. Res.*, **103,** 32 277–32 290.

Pidgeon, C. R., and S. D. Smith, 1964: Resolving power of multilayer films in nonparallel light. *J. Opt. Soc. Amer.*, **54,** 1459–1466.

Press, W. H., B. P. Flannery, S. A. Teukolksy, and W. T. Vetterling, 1986: Root finding and nonlinear sets of equations. *Numerical Recipes: The Art of Scientific Computing,* Cambridge University Press, 254–259.

Rothman, L. S., and Coauthors, 1998: The HITRAN molecular spectroscopic database and HAWKS (HITRAN Atmospheric Workstation): 1996 Edition. *J. Quant. Spectrosc. Radiat. Trans.*, **60,** 665–710.

Schluessel, P., 1990: On the bulk-skin temperature difference and its impact on satellite remote sensing of sea surface temperature. *J. Geophys. Res.*, **95,** 13 341–13 356.

Taylor, F. W., 1983: Pressure modulator radiometry. G.A. Vanasse, Ed., Vol. 3, *Spectroscopic Techniques,* Academic Press, 137–197.

Tolton, B. T., and J. R. Drummond, 1997: Characterization of the length-modulated radiometer. *Appl. Opt.*, **36,** 5409–5419.

Wang, J., J. C. Gille, P. L. Bailey, J. R. Drummond, and L. Pan, 1999: Instrument sensitivity and error analysis for the remote sensing of tropospheric carbon monoxide by MOPITT. *J. Atmos. Oceanic. Technol.*, **16,** 465–474.

Warner, J., J. Gille, D. P. Edwards, D. Ziskin, M. Smith, P. Bailey, and L. Rokke, 2001: Cloud detection and clearing for the earth observing system Terra satellite Measurements of Pollution in the Troposphere (MOPITT) experiment. *Appl. Opt.*, **40,** 1269–1284.